Journal of Materials Chemistry A

ROYAL SOCIETY OF CHEMISTRY

PAPER

Cite this: J. Mater. Chem. A, 2021, 9, 23968

A 3D-printed integrated MXene-based evaporator with a vertical array structure for salt-resistant solar desalination†

Yi Yang,[a] Wei Fan, *[a] Shijia Yuan,[a] Jing Tian,[a] Guojie Chao[b] and Tianxi Liu *[ab]

Received 24th August 2021
Accepted 4th October 2021

DOI: 10.1039/d1ta07225k

rsc.li/materials-a

High photo-to-heat conversion efficiency and excellent desalination performance are both urgent requirements for solar evaporators in actual applications. However, due to the limitation of a single structure and material, the traditional 3D evaporator cannot achieve both high efficiency photo-to-heat conversion and rapid salt removal at the same time. Herein, we report a three-dimensional (3D) integrated evaporator using 3D printing technology, which combines polyimide/MXene (PIM) aerogel arrays as the upper layer and polyimide (PI) aerogel lattices as the bottom layer. The PIM aerogel arrays exhibit a high light absorption rate of 91.3%, and the array structure functions as effective thermal confinement that greatly prevents heat loss while allowing steam to escape into the air. The PI aerogel lattices can form multi-directional mass transfer channels for fast water transport and enable rapid salt particle dissolution, thus inhibiting salt accumulation. Consequently, the 3D integrated evaporator displays both a remarkable photo-to-heat conversion efficiency of 99.7% and superior desalination performance under 1 sun illumination. This paper presents a novel insight for designing salt-resistant solar evaporation systems and can help to overcome the dilemma of water scarcity.

Introduction

Coupled with the increasingly serious problems such as uneven distribution of water and water pollution, fresh water shortage has become an urgent problem.[1,2] Under these circumstances, scientists have come up with using solar-driven steam generation to purify wastewater or seawater to get more fresh water for conquering these problems. However, traditional solar evaporators directly contact with bulk water, and heat will dissipate into the entire bulk water, which inevitably causes unnecessary heat/energy loss and results in low conversion efficiency. Therefore, an interfacial solar evaporation system that confines heat at the air–water interface is more meaningful and energy-efficient to increase solar steam generation efficiency.[3–7]

A typical interfacial solar evaporation system consists of the following parts: a light absorption layer, a water transport channel, and a salt removal region. Most of the interfacial solar evaporators are designed into three-dimensional (3D) structures (such as flower, aerogel and wood), which can simultaneously achieve efficient light absorption and water transport.[8–10] For instance, Fan *et al.* reported a unique solar steam system made of a 3D origami polypyrrole–paper composite. Compared with the two-dimensional (2D) structure, the unique 3D structure can improve light absorption to 99% and provide a remarkable evaporation rate of 2.12 kg m^{-2} h^{-1}.[11] Quan's team synthesized a MXene aerogel with a vertical array structure and found that the aerogel had competitive advantages in capillary water transport and vapor escape, which displayed a high evaporation efficiency (87%) and constant evaporation rate (~1.46 kg m^{-2} h^{-1}).[12] Yao and coworkers drilled an arrayed channel within a wood structure to create a self-regenerating solar evaporator that demonstrated excellent desalting capacity.[13] All of the 3D structures show higher evaporation efficiency and better desalination capacity than 2D structures.[14–18] However, due to the limitation of a single structure and material, the traditional 3D evaporator cannot achieve both high efficiency photo-to-heat conversion and rapid salt removal in the same system, which hinders its practical applications. Therefore, pursuing a reliable strategy to fabricate a 3D integrated evaporator with multiple materials/structures for both efficient photo-to-heat conversion efficiency and excellent salt removal is of great significance.

3D printing, as a typical additive manufacturing technology, displays unique advantages of a high degree of freedom in 3D structure design and has been extensively concerned in electrical, medical and environmental engineering applications.[19–24] Using this technology, evaporators can be fabricated into

[a]State Key Laboratory for Modification of Chemical Fibers and Polymer Materials, College of Materials Science and Engineering, Donghua University, Shanghai 201620, P. R. China. E-mail: weifan@dhu.edu.cn; txliu@fudan.edu.cn; txliu@dhu.edu.cn

[b]Key Laboratory of Synthetic and Biological Colloids, Ministry of Education, School of Chemical and Material Engineering, Jiangnan University, Wuxi 214122, P. R. China

† Electronic supplementary information (ESI) available. See DOI: 10.1039/d1ta07225k

arbitrary structures, and the structures can be adjusted and controlled *via* 3D printing technology to obtain optimal performance. For example, Hu's team used a 3D printer to create an integrated evaporator, which not only enables high broadband light absorption (97%), but also achieves heat localization.[25] In addition, they also fabricated an evaporator with a jellyfish-like structure to suppress heat dissipation and enable solar desalination.[26] Lu *et al.* designed a cone-shaped Janus evaporator by 3D printing technology, which provides a large evaporative surface for evaporation (1.73 kg m^{-2} h^{-1}) and an efficient way for desalination.[27] However, 3D printing ink needs to have certain rheological properties, and it is found that few photo-to-heat conversion materials can meet the requirements, which limits the further development of 3D printing technology in solar evaporation systems. As a new 2D material, an MXene presents a remarkable photo-to-heat conversion efficiency of 100%, which has been substantiated with great potential for solar desalination.[28–30] However, an MXene-based evaporator fabricated by 3D printing technology has not yet been reported. Although previous studies have reported MXene laminar membranes or aerogels as efficient solar evaporators, the tight or irregular porous structure may impede fast water transport, thus resulting in low photo-to-heat conversion efficiency. In addition, a few-layered MXene exhibited weak interconnection and easy overlapping, which makes it difficult to form a stable colloid state for printing. Till now, constructing a high performance MXene-based evaporator *via* 3D printing has remained a massive challenge.

In this work, we report a 3D integrated MXene-based evaporator *via* 3D printing with vertical array structures as the upper layer and lattice structures as the bottom layer. The upper polyimide/MXene (PIM) aerogel arrays exhibit a high light absorption rate of 91.3% and function as an effective thermal confinement that greatly prevents heat loss. The bottom polyimide (PI) aerogel lattices can form multi-directional mass transfer channels for fast water transport and enable rapid salt dissolution thus inhibiting salt accumulation. Consequently, the 3D integrated evaporator with the PIM aerogel arrays and the PI aerogel lattices exhibits a high evaporation rate of 2.17 kg m^{-2} h^{-1} and a high efficiency of 99.7%, as well as excellent seawater desalination performance. The 3D integrated evaporator is demonstrated with great potential in water purification and seawater desalination, which could present a novel insight for designing salt-resistant solar desalination systems.

Results and discussion

Fabrication and morphology of the 3D integrated evaporator

A 3D integrated evaporator combining vertical array and lattice structures was fabricated using layer-by-layer 3D printing, and the preparation process is schematically described in Fig. 1a. Lattice structured polyamic acid (PAA) layers were first printed, and subsequently PAA/MXene arrays were vertically printed on the top of the PAA layers. After conducting freeze-drying and thermal imidization treatment, the integrated polyimide/polyimide–MXene (PI/PIM) aerogel was obtained. Here, the lattice holes were generated by the 3D printed lattice structure and the aerogel pores were traces of sublimated ice crystals from freeze-drying, thus forming a highly porous structure in the microfilaments. During the 3D printing process, the rheological properties of the inks play a crucial role. The ideal ink must be easily extruded from the syringes under appropriate pressure and keep a stable shape after printing. However, the few-layered MXene exhibited weak interconnection and easy overlapping (Fig. S1†), which makes it difficult to form a stable colloid state at low concentrations to meet the requirements of printing. By adding PAA salt to the homogeneous MXene suspension, a strong three-dimensional network structure was formed between the PAA chains and MXene sheets through hydrogen bonding, which makes PAA/MXene exhibit a stable gel-state (Fig. S2†). From the viscosity-shear rate diagram in Fig. 1b, it can be clearly seen that both PAA and PAA/MXene inks exhibit a non-Newtonian behavior of shear thinning, implying that the viscosity decreases with increasing shear rates, which enables the inks to be smoothly extruded from the syringe. Fig. 1c displays the storage modulus (G') and loss modulus (G'') variations of the PAA and PAA/MXene inks with the shear stress increasing. Both inks exhibit gel properties with G' higher than G'' at low shear stress, which will facilitate the formability of inks. Therefore, a 3D integrated evaporator can be facilely designed *via* 3D printing using the PAA and PAA/MXene inks. Fig. 1d demonstrates the ultra-light characteristic of the 3D integrated evaporator. Other complex structures, such as pyramid and honeycomb structures, can also be produced by 3D printing (Fig. S3†).

The above inks were printed in a certain route to construct 3D integrated evaporator, which consists of upper vertical array and bottom lattice structures (Fig. 1e). The upper vertical arrays allow multiple reflections of light inside to enhance absorption, create heat confinement areas and prevent heat loss while allowing steam to escape into the air. The bottom PI aerogel lattices can form multi-directional mass transfer channels for fast water transport through the well-patterned porous microfilaments, and enable rapid salt dissolution through lattice holes, thus inhibiting salt accumulation. Therefore, this 3D integrated evaporator with a perfectly designed structure shows great potential for solar desalination.

In order to further elaborate the 3D integrated evaporator, we characterized each part of the 3D integrated evaporator with scanning electron microscopy (SEM). The upper layer is a vertical array structure composed of PIM aerogel (Fig. 2a). The corresponding SEM image in Fig. 2b shows that the arrays are formed by PIM aerogel microfilaments (about 200 μm in diameter), which are tightly stacked to facilitate the formation of thermal barriers to inhibit heat loss. The SEM image under higher magnification (Fig. 2c) further reveals the porous architectures of the PIM aerogel, and the MXene sheet is tightly wrapped by the PI matrix as shown in the transmittance electron microscopy (TEM) image in the inset, which effectively avoided the oxidation of the MXene. In addition, the existence of this porous structure allows steam to escape unimpededly during the solar steam generation process. The interface layer shows strong binding between the PIM aerogel arrays and the PI aerogel lattices (Fig. 2d), which is essential for the integrated

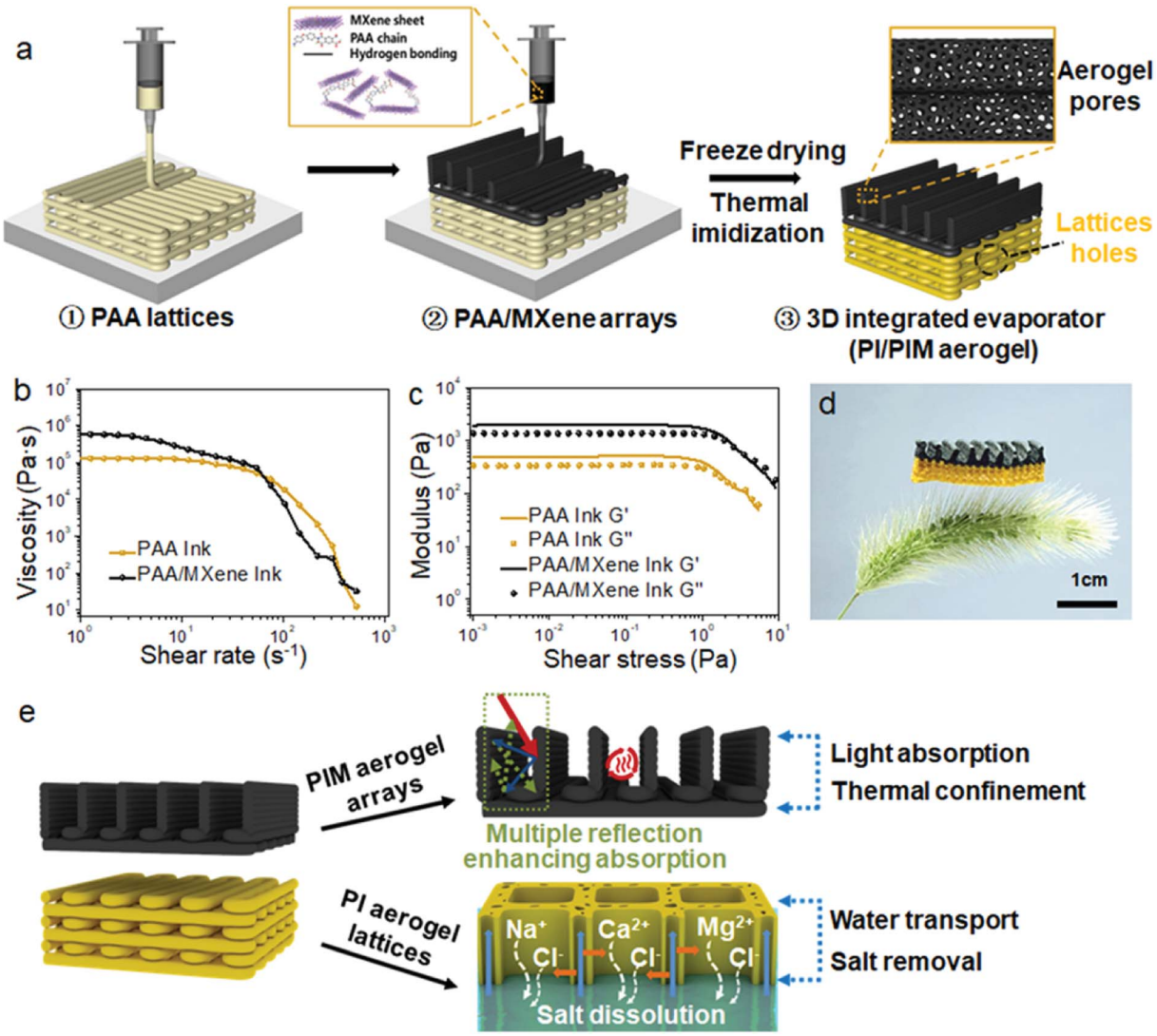

Fig. 1 Fabrication of the 3D integrated evaporator *via* 3D printing. (a) Schematic depicting the 3D printing process of the 3D integrated evaporator. (b) Apparent viscosity of PAA and PAA/MXene inks as a function of shear rate. (c) Storage modulus (G') and loss modulus (G'') of PAA and PAA/MXene inks as a function of shear stress. (d) Digital images demonstrating the light weight of the 3D integrated evaporator. (e) The structure diagram of the 3D integrated evaporator, showing the function of PIM vertical arrays and PI lattice structures.

structure, ensuring rapid water transport in microchannels from bottom to top (Fig. 2e and f). The bottom layer is a lattice structure composed of PI aerogel (Fig. 2g). The SEM image displays the lattice hole structure under low magnification (Fig. 2h). Under high magnification (Fig. 2i), the crisscrossed pattern of microfilaments displays a highly porous structure, which can provide interconnected channels for continuous and rapid water transport.

Structural design and optimization of the 3D integrated evaporator

In order to obtain a higher evaporation rate, the absorption layer of the evaporator is designed into an array structure using 3D printing technology. The vertical array structure can efficiently absorb sunlight, creating heat confinement areas and preventing heat loss. As illustrated in Fig. 3a, multiple reflection of light (indicated by green arrows) can occur in the vertical array structure, while only single reflection (indicated by blue arrows) can occur on the arrayless structure, indicating that the vertical array structure can absorb the incident light by multiple reflections. The light absorption capacity of the array structure was explored by using a UV-vis Spectrometer (Fig. 3b and c). The results reveal that the light transmittance of the array structure is almost zero, and the reflectance is only 8.7% in the visible region (the range of 500–2500 nm), which is lower than that of the arrayless structure (Fig. S4†), presenting an excellent light absorption performance. Since a thermal confinement ability has a great influence on the evaporation rate, we further compared the surface temperature of the arrayless structure and the array structure under both dry and wet conditions (Fig. 3d). According to the thermal infrared image, the surface temperature of the 3D integrated evaporator under wet

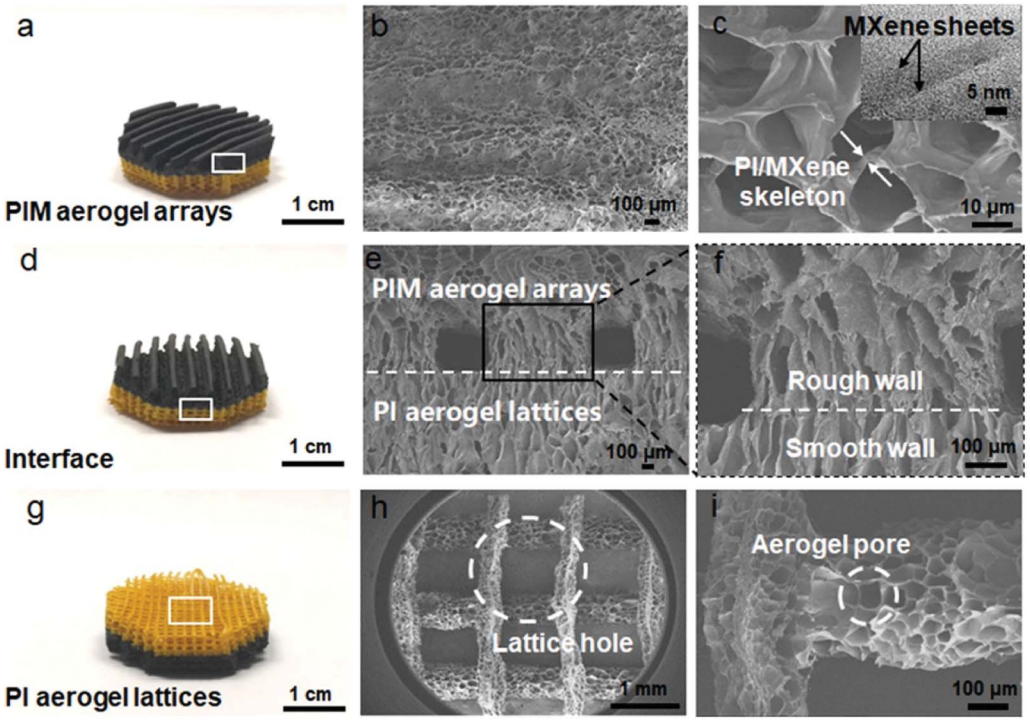

Fig. 2 Morphologies of the 3D integrated evaporator. (a) The upper layer of the 3D integrated evaporator. Corresponding SEM image of the upper arrays at (b) low and (c) high magnification. Inset: TEM image of the PIM skeleton. (d) The interface layer of the 3D integrated evaporator and (e and f) corresponding SEM images showing the interface between PIM aerogel arrays and PI aerogel lattices. (g) The bottom layer of the 3D integrated evaporator and (h and i) corresponding SEM image of the PI aerogel lattice showing interconnected microchannels.

conditions is lower than that under dry conditions due to the high thermal enthalpy of water (~623.65 kJ kg^{-1} at 48 °C), but the surface temperature of the array structure is higher than that of the arrayless structure in general. This is because the narrow gaps between vertical arrays can not only block the radiation loss to the surrounding, but also greatly reduce convective heat loss. Moreover, the thermal conductivity of the two structures has been considered to explain this phenomenon. As illustrated in Fig. 3e, the thermal conductivity of the array structure is lower than that of the arrayless structure under both dry and wet conditions, indicating that the array structure has a slow heat exchange capacity with the external environment, which greatly reduces the heat loss.

Since the array structure plays a positive role in light absorption and thermal confinement, the height of PIM aerogel arrays and gaps between arrays were regulated by 3D printing to optimize the evaporation performance. Fig. S5† shows the cumulative weight loss and the water evaporation rates of the array structure with different array gaps and heights under 1 sun illumination. Compared with the 3D integrated evaporator with the arrayless structure, the evaporation efficiency of the 3D integrated evaporator with the array structure is much higher. Moreover, the array structure with a gap of 3 mm and a height of 3.5 mm shows the optimized water weight loss and evaporation efficiency. This is because the denser and taller vertical arrays provide more places for multiple reflected light, thus absorbing more sunlight for photo-to-heat conversion, leading to higher evaporation efficiency.

The bottom layer is designed into a lattice structure by 3D printing and each microfilament is porous due to the freeze-drying that causes ice crystals to sublimate, which can form multi-directional mass transfer channels for fast water transport and salt dissolution. As illustrated in Fig. 4a, water is transported upward along the PI aerogel microfilaments under the capillary force and the desalting process of the lattice structure can be explained as spontaneous salt exchange between lattice holes and aerogel pores. As the water flux is influenced by the diameter,[31] a salt concentration gradient will be formed between the lattice holes and the aerogel pores, resulting in salt particles being transferred from the aerogel pores with a high salt concentration to lattice holes with a low salt concentration, thus allowing salt dissolution and inhibiting salt particle accumulation. During the evaporation process, the wettability of the material surface is necessary to enhance efficient water supply. The simulated seawater contact angles of the PI aerogel and PIM aerogel are 38.2° and 26.4°, respectively (Fig. S6†), showing the good hydrophilicity of the 3D integrated evaporator, which is beneficial for efficient water adsorption. To highlight the water adsorption capacity of lattice structures, the bottom layer without a lattice structure is fabricated for comparison. Dyed water is used here for easy observation, and the dyed water contact angles of the PI aerogel and PIM aerogel are similar to those of seawater (Fig. S7†), indicating similar wettability. Fig. 4b shows the heights of dyed water transport in PI aerogel strips with latticeless and lattice structures within 10 s, and the latter is obviously higher. The corresponding

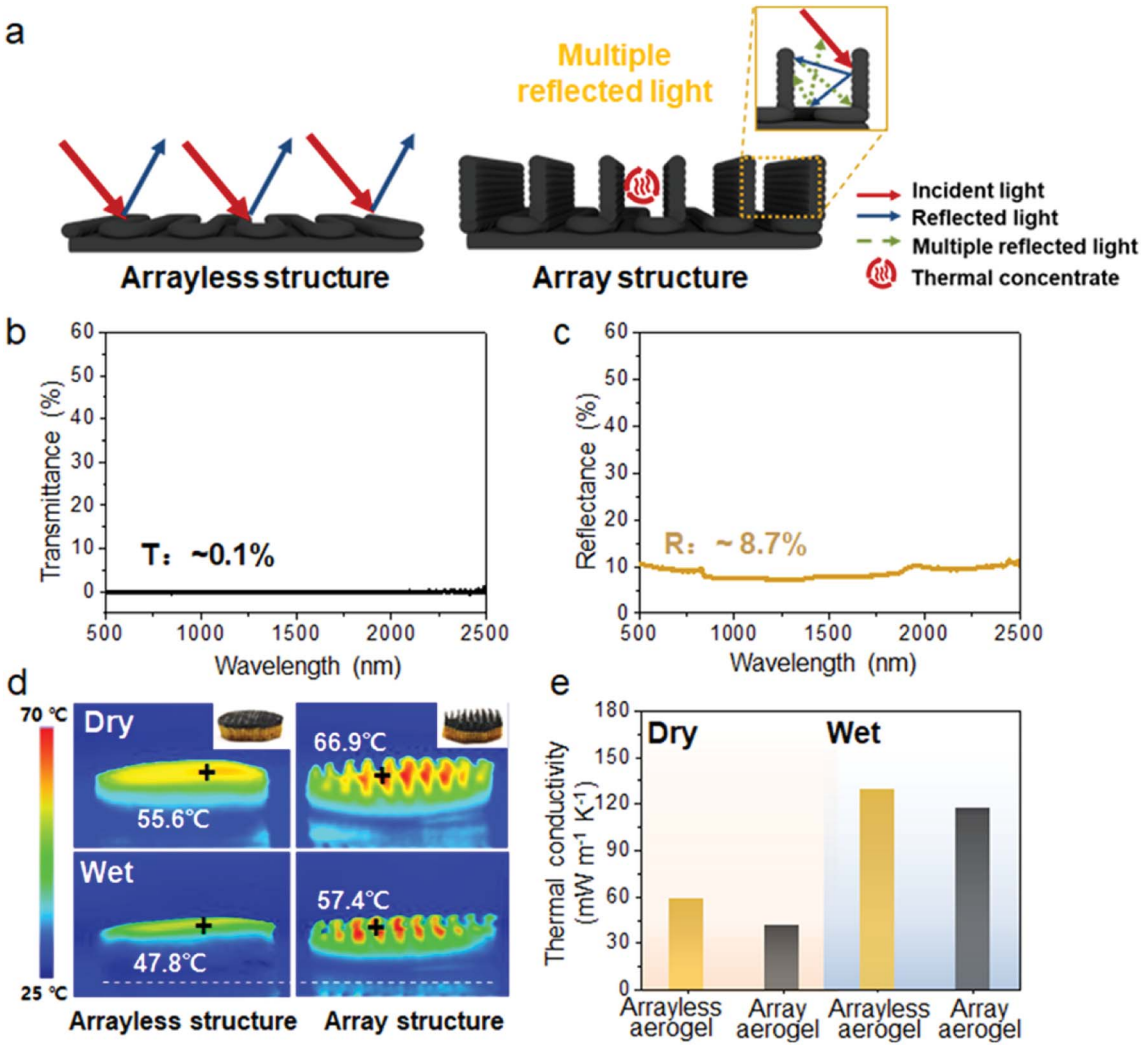

Fig. 3 Light absorption and heat confinement capacity of the vertical array structure. (a) Schematic illustration of light absorption of the PIM aerogel with arrayless and array structures. (b) Transmittance and (c) reflectance spectra of the PIM aerogel with the array structure. The results show that the light transmittance and reflectance are extremely low at 500–2500 nm. (d) Thermal infrared images and (e) thermal conductivity of the PIM aerogel with arrayless and array structures under dry and wet conditions.

adsorption process is also recorded in Video S1.† The same results are also displayed in the variation curve of the fluidic height over time (Fig. 4c). The water adsorption rate of the PI aerogel strip with a lattice structure can reach 1.35 mm s^{-1}, which is almost 7 times that of the latticeless structure. Subsequently, we further investigated the water adsorption capacity of the 3D integrated evaporator, and the results are shown in Fig. S8a.† It was observed that the dry paper placed at the top of the evaporator quickly became wet when the evaporator was placed on water, indicating that water could be transferred easily from the bottom to the top of the evaporator. Moreover, it showed a certain stability of water adsorption under cyclic tests. Besides, the porosity of the 3D integrated evaporator can be characterized by the specific weight before and after water adsorption. After full water adsorption, the density of the evaporator increased from 0.0697 g cm^{-3} to 0.5704 g cm^{-3}, and the porosity can be inferred to be 50.07% (Fig. S8b†).

The salt-removal capability of the 3D integrated evaporator with different structures was measured in 20 wt% NaCl solution under 1 sun illumination. It can be observed that salt particles precipitate on the surface of the latticeless structure within 6 hours, while the surface of the lattice structure was still clean after continuously illuminating for 24 h (Fig. 4d), indicating the excellent salt-removal capability of the 3D integrated evaporator with the lattice structure. We further calculated the cumulative weight loss and the water evaporation rates of the 3D integrated evaporator with latticeless and lattice structures. As illustrated in Fig. 4e and f, the 3D integrated evaporator with the lattice structure promotes the cumulative weight loss to 0.85 kg m^{-2} from 0.47 kg m^{-2}, and the maximum evaporation rate is 2.17 kg m^{-2} h^{-1}. In addition, the heights of the lattice structure were adjusted through 3D printing technology to obtain the best evaporation performance. It was found that the evaporation rate increases with the increased lattice height, and an optimized

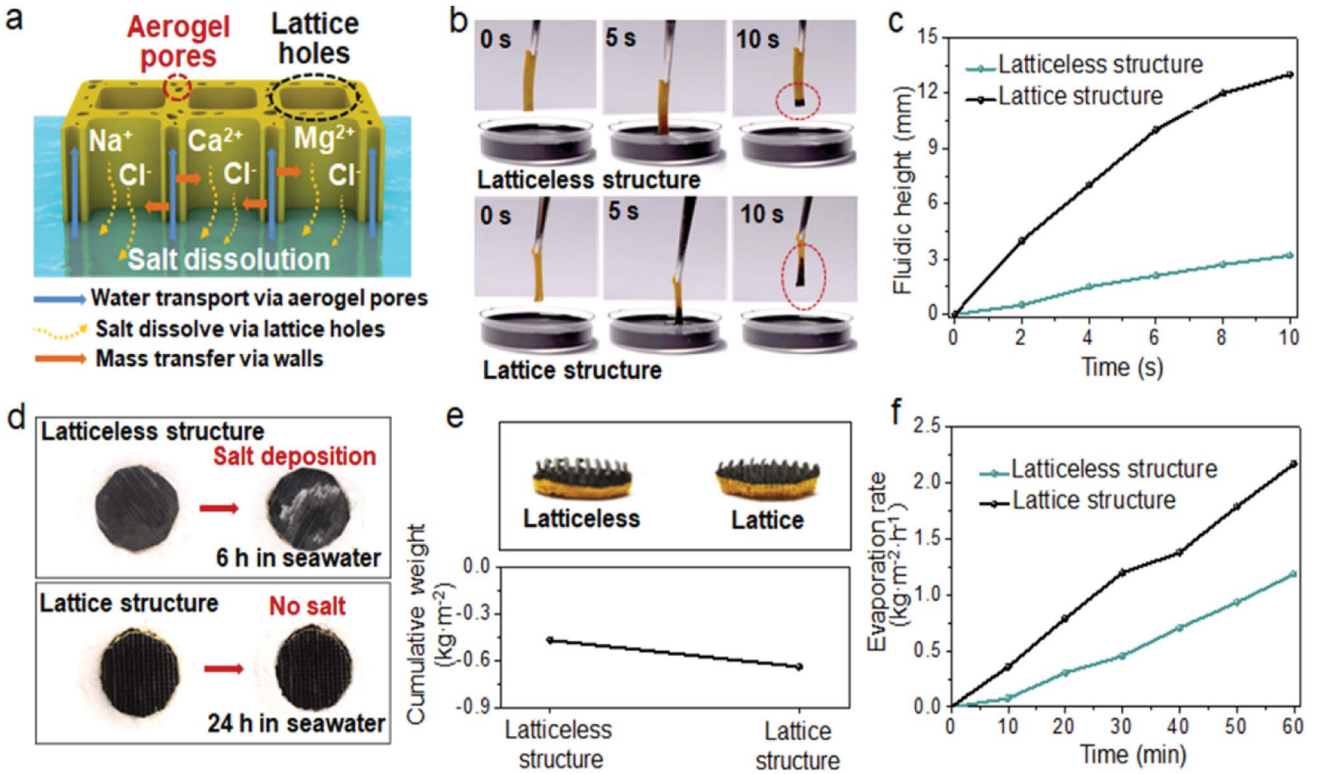

Fig. 4 Water adsorption and salt dissolution performance of the lattice structure. (a) Schematic illustration showing the salt-dissolve mechanism of the PI aerogel lattice. (b) Water transport image and (c) curves of the fluidic height over time of PI aerogel strips with/without the lattice structure. (d) Surface images of the 3D integrated evaporator with/without the lattice structure before and after floating on NaCl solution under 1 sun illumination. (e) The cumulative weight loss and (f) water evaporation rates of the 3D integrated evaporator with/without the lattice structure under 1 sun illumination.

lattice height of 3 mm was selected in the following work (Fig. S9†).

Water evaporation and desalination performance of the 3D integrated evaporator

The 3D integrated evaporator as a desalination setup is shown in Fig. 5a. The PI aerogel lattices pump water continuously to the upper layer and rapidly removes salt from channels, while the PIM aerogel arrays convert the absorbed light into heat that is used to heat the water for producing more steam. Then, the condensate water flows down the glass walls and fresh water can be collected through grooves. The surface temperature variation of the 3D integrated evaporator and pure water was measured by using an infrared camera (Fig. 5b). Under stable illumination, the surface temperature of the 3D integrated evaporator increases rapidly within 5 min and remains at 49.8 °C for a long time, while pure water can only reach 35.6 °C. The temperature change with time can be seen intuitively in Fig. 5c. The higher surface temperature of the 3D integrated evaporator indicates its excellent thermal confinement performance. Fig. 5d shows the relationship between the cumulative weight loss of the system and illumination time. It is noted that the cumulative weight loss of the system dramatically varies with increased time and the 3D integrated evaporator exhibits a higher weight loss than that of pure water. Fig. 5e shows the evaporation rate under 10 cycles, showing that the evaporation rate of the 3D integrated evaporator is stable at ~2 kg m^{-2} h^{-1}. Furthermore, we also tested the evaporation rates of the 3D integrated evaporator in a dark field for excluding the effect of spontaneous water evaporation (Fig. S10†), and the photo-to-heat conversion efficiency of the evaporator is calculated to be 99.7%, which is superior to those of previously reported evaporators, such as GO,[25,26,32] cellulose,[11,15,29] carbon[16,27,33–37] and MXenes[12,28,38] (Fig. 5f).

Subsequently, we also studied the long-term stability and practicability of the 3D integrated evaporator in seawater. Natural seawater from Weihai, China was used as the sample for the desalination test. As shown in Fig. 5g, the 3D integrated evaporator can achieve a stable evaporation rate of 1.8–1.9 kg m^{-2} h^{-1} under continuous illumination for 100 hours, indicating its good durability. Fig. S11a† exhibits a digital image of the 3D integrated evaporator tested in an actual environment. Notably, the condensation of droplets can be observed in the collector, but the measured water evaporation rate is slightly lower than that in the lab. This is to be expected because outdoor conditions are subjected to varying incident solar flux (Fig. S11b†), which results in a decreased evaporation rate. The concentrations of five common ions (Na^+, K^+, Ca^{2+}, Mg^{2+} and B^{3+}) in seawater, direct drinking water, mineral water and distilled water are compared. It is found that the ion

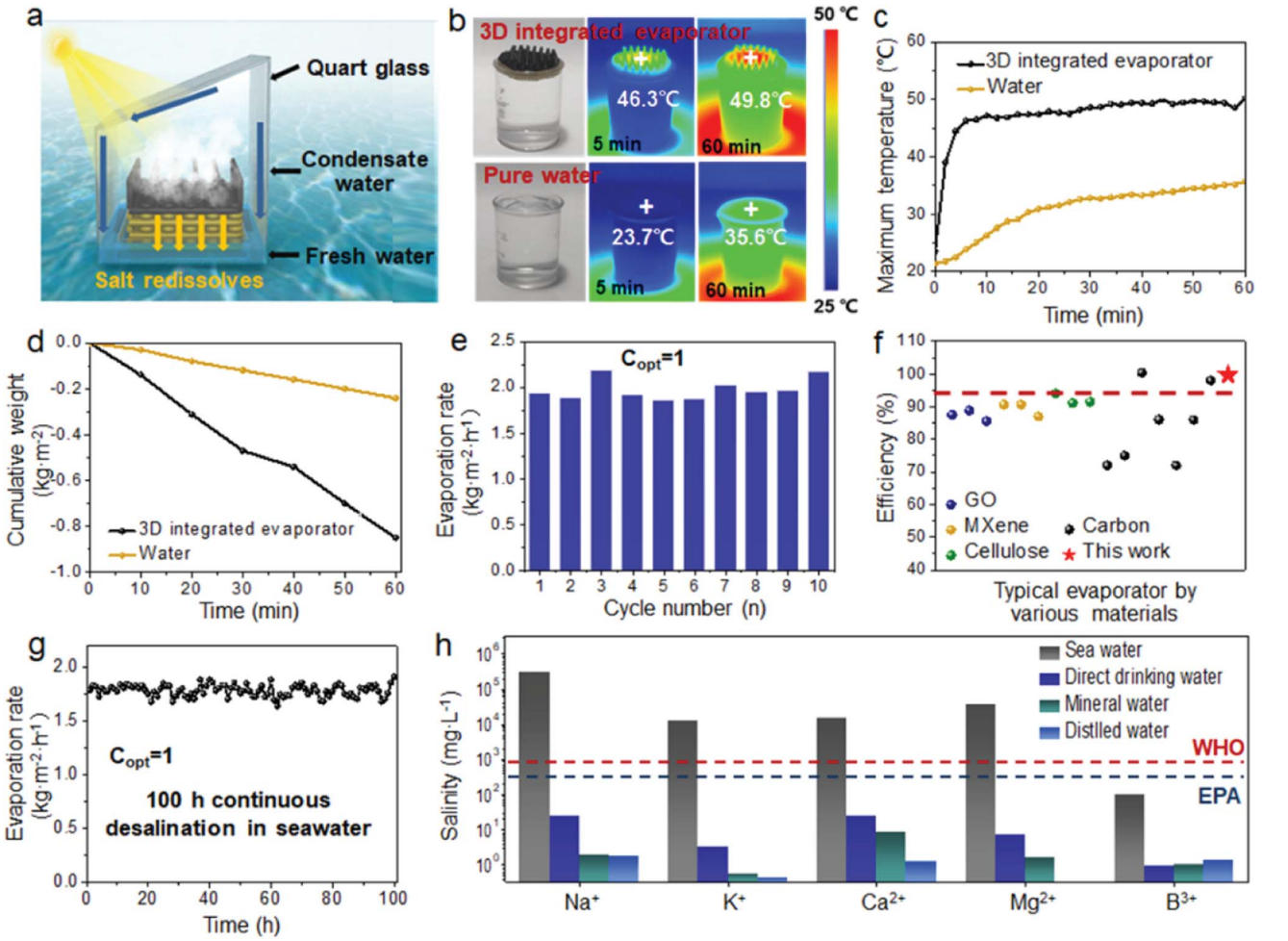

Fig. 5 Water evaporation and desalination performance of the 3D integrated evaporator. (a) Schematic diagram showing the evaporation process of the 3D integrated evaporator as a desalination setup. (b) Thermal infrared images and (c) surface temperature curves of the 3D integrated evaporator and pure water at different times. (d) The cumulative weight loss of the 3D integrated evaporator and pure water. (e) The evaporation rate of the 3D integrated evaporator under 10 cycles (C_{opt} as sunlight intensity, each irradiation for 60 min). (f) Comparison of the evaporation efficiency of this work with that of previously reported studies under 1 sun illumination. (g) The evaporation rates of the 3D integrated evaporator for 100 h in seawater (1 sun illumination, each irradiation for 60 min). (h) The concentration of five metal ions in seawater, direct drinking water, mineral water and distilled water.

concentration of distilled water is not only about four orders of magnitude lower than that of the initial seawater, but also lower than that of both direct drinking water and mineral water, and in line with the ion concentration limitation of the World Health Organization (WHO) and U.S. Environmental Protection Agency (USEPA) for drinking criteria. Therefore, the 3D integrated evaporator shows great potential in practical water purification and seawater desalination.

Conclusions

In short, we used a 3D printer to produce an integrated MXene-based evaporator with a vertical array structure as the upper layer and a lattice structure as the bottom layer, which exhibits good evaporation efficiency and superior salt-resistant desalination performance. By designing the upper polyimide/MXene (PIM) aerogel into a vertical array structure, the incident light can be reflected multiple times inside the structure to enhance light absorption, and a thermal barrier is formed to inhibit heat loss. The bottom polyimide (PI) aerogel was designed into a lattice structure, which can form multi-directional mass transfer channels for fast water transport with low transport resistance, and enable rapid salt particle dissolution and inhibit salt accumulation. Finally, the 3D integrated evaporator exhibits a high evaporation rate of 2.17 kg m^{-2} h^{-1} and efficiency of 99.7%, respectively. In the actual seawater desalination test, the 3D integrated evaporator is demonstrated to be highly stable with a good evaporation rate for 100 hours, and the ion concentration of five common ions in distilled water is much lower than the value of the WHO and USEPA for safe drinking water. Considering the huge application opportunities of solar evaporators in the environment and the convenience of manufacturing approaches, the integrated MXene-based evaporator prepared by 3D printing technology is expected to be

used in water purification, seawater desalination and other fields.

Experimental sections

Preparation of the PAA and PAA/MXene inks

PAA ink. 0.8 g polyamic acid (PAA) precursors (synthesized in our previous work[39]) and triethylamine (TEA) were dissolved in 10 ml DI water, and a uniform PAA ink was obtained after magnetic stirring for 4 hours.

PAA/MXene ink. Few-layered MXenes were fabricated by etching Ti_3AlC_2 according to previous work.[40] A stable MXene suspension was obtained by dispersing 0.5 g MXene ($Ti_3C_2T_x$) in DI water with ultrasonication. Then a certain amount of PAA and TEA was added to the MXene suspension, and a uniform PAA/MXene ink was obtained after magnetic stirring for 6 hours.

3D printing process and construction of the 3D integrated evaporator

The two inks were loaded into separate syringes with an inner diameter of 400 μm, respectively. Then the syringe filled with the ink was installed on a dispensing machine for printing under a certain programming path (RZC-30WK, China). During the printing process, the inks were extruded from the syringes at a pressure of about 300 kPa and printed at a speed of 4 mm s^{-1}. After printing, the 3D integrated evaporator with polyimide–MXene (PIM) aerogel arrays and polyimide (PI) aerogel lattices was obtained by freeze-drying and thermally imidized at 300 °C in an argon atmosphere.

Characterization

The microstructures of the aerogels were investigated by using a scanning electron microscope (SEM, Ultra55). The MXene sheets were analyzed by transmission electron microscopy (TEM, JEM-2100, JEOL). The XRD spectra of MAX(Ti_3AlC_2), MXene and PIM powders were characterized by X-ray diffraction (DX-2700BH, China). The rheological properties of the inks were measured by using a modular compact rheometer (MCR302, China). The reflectance and transmittance spectra in the range of 500–2500 nm were collected by using a UV-vis Spectrometer (UV3600, Japan). All samples were placed in a Vacuum plasma processor (VP-T3, China) for hydrophilic treatment. The hydrophilicity of the PI aerogel and PIM aerogel was analyzed by using a dynamic contact angle testing instrument (OSA200, Germany). Thermographic images and temperature curves at different times were recorded by using an infrared camera (FOTRIC 226s, USA). Thermal diffusivity is tested by using a Hot Disk TPS 2500 S instrument (Hot Disk AB, Sweden). The ion concentrations were detected by using a plasma spectrometer (Prodigy-ICP, USA).

Solar steam generation and desalination experiment

The simulated sunlight was provided by a solar simulator (Zennium CIMPS-1) with an optical filter. The 3D integrated evaporator was placed in a 25 mm diameter beaker containing DI water for testing. Since the projected area of the array structure under sunlight is approximately the sample surface area, the sample surface area is regarded as the light absorption area. The cumulative weight changes were measured by using a high precision electronic balance (CNW, accuracy: 0.01 g) and recorded in real time. In all laboratory experiments, the simulated sunlight was vertically incident to the top of the evaporator with the room temperature of 25 °C and environmental humidity of 50%. The diameter of the experiment samples was between 2.2 to 2.3 mm.

The solar thermal conversion efficiency, η, is measured according to the following equation:[38]

$$\eta = \dot{m}h_{LV}/I$$

where $\dot{m}$ is the difference between the evaporation efficiency under light and dark, h_{LV} represents the enthalpy of the liquid–gas phase, and I is the power density of incident light. It is known that h_{LV} is ~2382 kJ kg^{-1} at 49.5 °C, and the evaporation efficiency of the 3D integrated evaporator is 0.66 kg m^{-2} h^{-1} under a dark field.

Conflicts of interest

The authors declare no conflict of interest.

Acknowledgements

The authors are grateful for the financial support from the National Natural Science Foundation of China (52073053), the Fundamental Research Funds for the Central Universities (2232019A3-03), Shanghai Rising-Star Program (21QA1400300), Innovation Program of Shanghai Municipal Education Commission (2021-01-07-00-03-E00108), Science and Technology Commission of Shanghai Municipality (20520741100), and Shanghai Municipal Education Commission (17CG33).

References

1 P. Zhang, Q. Liao, H. Yao, Y. Huang, H. Cheng and L. Qu, *Energy Storage Mater.*, 2019, **18**, 429–446.
2 M. Elimelech and W. A. Phillip, *Science*, 2011, **333**, 712–717.
3 F. Zhao, X. Y. Zhou, Y. Shi, X. Qian, M. Alexander, X. P. Zhao, S. Mendez, R. G. Yang, L. T. Qu and G. H. Yu, *Nat. Nanotechnol.*, 2018, **13**, 489–495.
4 L. L. Zhu, M. M. Gao, C. K. N. Peh and G. W. Ho, *Nano Energy*, 2019, **57**, 507–518.
5 X. Y. Zhou, F. Zhao, Y. H. Guo, Y. Zhang and G. H. Yu, *Energy Environ. Sci.*, 2018, **11**, 1985–1992.
6 Y. Ito, Y. Tanabe, J. H. Han, T. Fujita, K. Tanigaki and M. W. Chen, *Adv. Mater.*, 2015, **27**, 4302–4307.
7 G. H. Liu, T. Chen, J. L. Xu, G. Li and K. Y. Wang, *J. Mater. Chem. A.*, 2020, **8**, 513–531.
8 Y. W. Yang, H. Y. Zhao, Z. Y. Yin, J. Q. Zhao, X. T. Yin, N. Li, D. D. Yin, Y. N. Li, B. Lei, Y. P. Du and W. Que, *Mater. Horiz.*, 2018, **5**, 1143–1150.

9 J. X. Chen, B. Li, G. X. Hu, R. Aleisa, S. Lei, F. Yang, D. L. Liu, F. L. Lyu, M. Z. Wang, X. W. Ge, F. Qian, Q. Zhang and Y. D. Yin, *Nano Lett.*, 2020, **20**, 6051–6058.

10 H. P. Sun, Q. Zhou, Q. H. Zhao, L. M. Shi, D. Wang and T. Mei, *Compos. Commun.*, 2019, **13**, 151–155.

11 W. G. Li, Z. Li, K. Bertelsmann and D. E. Fan, *Adv. Mater.*, 2019, **31**, 1900720.

12 Q. Zhang, G. Yi, Z. Fu, H. T. Yu, S. Chen and X. Quan, *ACS Nano*, 2019, **13**, 13196–13207.

13 X. F. Zhang, Z. G. Wang, L. Song, Y. Feng and J. F. Yao, *Desalination*, 2020, **496**, 114727.

14 G. L. Chen, N. Zhang, N. Li, L. M. Yu and X. F. Xu, *Adv. Mater. Interfaces*, 2019, **7**, 1901715.

15 Y. C. Wang, C. Z. Wang, X. J. Song, M. H. Huang, S. K. Megarajan, S. F. Shaukat and H. Q. Jiang, *J. Mater. Chem. A.*, 2018, **6**, 9874–9881.

16 N. Xu, X. Z. Hu, W. C. Xu, X. Q. Li, L. Zhou, S. N. Zhu and J. Zhu, *Adv. Mater.*, 2017, **29**, 1606762.

17 C. Tu, W. F. Cai, X. Chen, X. L. Ouyang, H. Zhang and Z. Zhang, *Small*, 2019, **15**, 1902070.

18 X. Q. Li, J. L. Li, J. Y. Lu, N. Xu, C. L. Chen, X. Z. Min, B. Zhu, H. X. Li, L. Zhou, S. N. Zhu, T. J. Zhang and J. Zhu, *Joule*, 2018, **2**, 1331–1338.

19 B. Yao, S. Chandrasekaran, J. Zhang, W. Xiao, F. Qian, C. Zhu, E. B. Duoss, C. M. Spadaccini, M. A. Worsley and Y. Li, *Joule*, 2019, **3**, 459–470.

20 M. W. Peng, Z. Wen, L. J. Xie, J. Cheng, Z. Jia, D. L. Shi, H. J. Zeng, B. Zhao, Z. Q. Liang, T. Li and L. Jiang, *Adv. Mater.*, 2019, **31**, 1902930.

21 V. C. F. Li, C. K. Dunn, Z. Zhang, Y. L. Deng and H. J. Qi, *Sci. Rep.*, 2017, **7**, 8018.

22 P. L. Yan, E. Brown, Q. Su, J. Li, J. Wang, C. X. Xu, C. Zhou and D. Lin, *Small.*, 2017, **13**, 1701756.

23 Y. Wang, Z. W. Fan, H. Zhang, J. Guo, D. X. Yan, S. F. Wang, K. Dai and Z. M. Li, *Mater. Des.*, 2021, **197**, 109222.

24 J. L. Wang, S. Mubarak, D. Dhamodharan, N. Divakaran, L. X. Wu and X. Zhang, *Compos. Commun.*, 2020, **19**, 142–146.

25 Y. J. Li, T. T. Gao, Z. Yang, C. J. Chen, W. Luo, J. W. Song, E. Hitz, C. Jia, Y. B. Zhou, B. Y. Liu, B. Yang and L. B. Hu, *Adv. Mater.*, 2017, **29**, 1700981.

26 X. Q. Li, W. C. Xu, M. Y. Tang, L. Zhou, B. Zhu, S. N. Zhu and J. Zhu, *Proc. Natl. Acad. Sci. U. S. A.*, 2016, **113**, 13953–13958.

27 N. N. Cao, S. T. Lu, R. Yao, C. X. Liu, Q. Y. Xiong, W. Qin and X. H. Wu, *Chem. Eng. J.*, 2020, **397**, 125522.

28 X. Q. Fan, Y. Yang, X. L. Shi, Y. Liu, H. P. Liu, J. J. Liang and J. Wang, *Adv. Funct. Mater.*, 2020, 2007110.

29 J. X. Chen, Z. L. Li, F. L. Ni, W. X. Ouyang and X. S. Fang, *Mater. Horiz.*, 2020, **7**, 1828–1833.

30 R. Y. Li, L. B. Zhang, L. Shi and P. Wang, *ACS Nano*, 2017, **11**, 3752–3759.

31 Y. D. Kuang, C. J. Chen, S. M. He, E. M. Hitz, Y. Wang, W. T. Gan, R. Y. Mi and L. B. Hu, *Adv. Mater.*, 2019, **31**, 1900498.

32 Y. J. Li, T. T. Gao, Z. Yang, C. J. Chen, Y. D. Kuang, J. W. Song, C. Jia, E. M. Hitz, B. Yang and L. B. Hu, *Nano Energy*, 2017, **41**, 201–209.

33 C. Chang, P. Tao, B. W. Fu, J. L. Xu, C. Y. Song, J. B. Wu, W. Shang and T. Deng, *ACS Omega*, 2019, **4**, 3546–3555.

34 L. Wu, Z. C. Dong, Z. R. Cai, T. Ganapathy, N. X. Fang, C. X. Li, C. L. Yu, Y. Zhang and Y. L. Song, *Nat. Commun.*, 2020, **11**, 521.

35 T. J. Chen, H. Xie, X. Qiao, S. Q. Hao, Z. Z. Wu, D. Sun, Z. Y. Liu, F. Cao, B. H. Wu and X. L. Fang, *ACS Appl. Mater. Interfaces*, 2020, **12**, 50397–50405.

36 P. Sun, W. Zhang, I. Zada, Y. X. Zhang, J. J. Gu, Q. L. Liu, H. L. Su, D. Pantelić, B. Jelenković and D. Zhang, *ACS Appl. Mater. Interfaces*, 2019, **12**, 2171–2179.

37 S. Chen, Z. Y. Sun, W. L. Xiang, C. Y. Shen, Z. Y. Wang, X. Y. Jia, J. Sun and C. J. Liu, *Nano Energy*, 2020, **76**, 104998.

38 X. Ming, A. K. Guo, Q. Zhang, Z. Z. Guo, F. Yu, B. F. Hou, Y. Wang, K. P. Homewood and X. B. Wang, *Carbon*, 2020, **167**, 285–295.

39 W. Fan, L. Z. Zuo, Y. F. Zhang, Y. Chen and T. X. Liu, *Compos. Sci. Technol.*, 2018, **156**, 186–191.

40 S. L. Zhang, P. F. Huang, J. L. Wang, Z. H. Zhuang, Z. Zhang and W. Q. Han, *J. Phys. Chem. Lett.*, 2020, **11**, 1247–1254.